BIOCHEMISTRY
including biophysical chemistry & molecular biology
Article

Biochemistry **2009,** *48,* 11231–11242 11231
DOI: 10.1021/bi901216s

Coupling of the Distal Hydrogen Bond Network to the Exogenous Ligand in Substrate-Bound, Resting State Human Heme Oxygenase†

Dungeng Peng,‡ Hiroshi Ogura,‡ Wenfeng Zhu,‡ Li-Hua Ma,‡ John P. Evans,§ Paul R. Ortiz de Montellano,§ and Gerd N. La Mar*,‡

‡*Department of Chemistry, University of California, Davis, California, 95616, and* §*Department of Pharmaceutical Chemistry, University of California, 600 16th Street, San Francisco, California 94158-2517*

Received July 16, 2009; Revised Manuscript Received October 19, 2009

ABSTRACT: Mammalian heme oxygenase (HO) possesses catalytically implicated distal ordered water molecules within an extended H-bond network, with one of the ordered water molecules (#1) providing a bridge between the iron-coordinated ligand and the catalytically critical Asp140, that, in turn, serves as an acceptor for the Tyr58 OH H-bond. The degree of H-bonding by the ligated water molecule and the coupling of this water molecule to the H-bond network are of current interest and are herein investigated by ^{1}H NMR. Two-dimensional NMR allowed sufficient assignments to provide both the H-bond strength and hyperfine shifts, the latter of which were used to quantify the magnetic anisotropy in both the ferric high-spin aquo and low-spin hydroxo complexes. The anisotropy in the aquo complex indicates that the H-bond donation to water #1 is marginally stronger than in a bacterial HO, while the anisotropy for the hydroxo complex reveals a conventional $(d_{xz}, d_{yz})^1$ ground state indicative of only moderate to weak H-bond acceptance by the ligated hydroxide. Mapping out the changes of the H-bond strengths in the network during the ligated water → hydroxide conversion by correcting for the effects of magnetic anisotropy reveals a very substantial change in H-bond strength for Tyr58 OH and lesser effects on nearby H-bonds. The effect of pH on the H-bonding network in human HO is much larger and transmitted much further from the iron than in a pathogenic bacterial HO. The implications for the HO mechanism of the H-bond of Tyr58 to Asp140 are discussed.

Heme oxygenase (HO)[1] is a widely distributed enzyme (*1*) that uses heme as a substrate and cofactor to cleave the heme via three intermediates (*2*−*6*), as depicted in Figure 1. HOs occur in at least two forms in humans, a constitutive isozyme, designated hHO-2, and an inducible hHO-1. Both are membrane-bound, although the majority of the structure and function studies of the more extensively studied hHO-1 have been carried out on a soluble recombinant construct from which the C-terminal membrane-anchor helix has been deleted (*7*). In mammals, all three products of the reaction are vital; biliverdin, upon reduction by biliverdin reductase, serves as a potent antioxidant (*8*), the liberated iron represents ∼97% of the daily requirement of iron (*9*), and CO serves as a neural messenger (*10*). Shorter, soluble HOs occur in plants and cyanobacteria where the biliverdin product is a precursor to light harvesting pigments (*11*) and in some pathogenic bacteria (*3*−*6*) where they are crucial for scavenging iron from the host. The reaction exhibits two properties of particular interest. It is highly regiospecific, cleaving a single *meso*-position, and the active species that attacks the unique *meso* position appears to result from homolytic, rather than the more common heterolytic, O−O bond cleavage of the Fe^{3+}−OOH unit (*5*, *12*−*15*); the latter reaction leads to the catalytically competent oxo−ferryl species common to the cytochromes P450 and peroxidases but inactive in HOs.

The factors that control stereoselectivity are reasonably well understood; the distal helix makes tight contacts with the distal heme face so as to block three of the four *meso* positions, and the distal helix backbone sterically tilts/orients the exogenous ligand (first O_2, then Fe−OOH) toward the fourth, unblocked *meso* position that is attacked (*16*−*20*). Variable stereoselectivity has been shown to arise from the detailed isomeric manner in which the substrate is seated within the conserved active site (*20*−*22*). The novel environmental influences in HOs that steer the Fe^{3+}−OOH unit toward homolytic, rather than heterolytic, O−O bond cleavage are less well understood. The former mechanism appears to be favored by the distal ligand interacting primarily with an ordered water molecule that is part of a series of ordered water molecules (*16*−*20*) within an extended H-bond network. The chemical shifts for several labile protons in this network exhibit strong low-field bias indicative of significant H-bonding (*23*−*27*).

While the various HOs share only limited sequence homology (*2*, *4*), they exhibit a unique, highly conserved fold consisting primarily of α-helices (*16*−*20*). There is less sequence and structural homology among the diverse HOs with respect to the distal H-bond network within which the catalytically implicated ordered water molecules are organized, although each HO exhibits (*16*−*20*) similarly ordered water molecules near the distal iron ligation site. In mammalian HOs (*16*, *17*), a key nonligated,

†This research was supported by grants from the National Institutes of Health, GM62830 (G.N.L.) and DK30297 (P.R.O.).

*To whom correspondence should be addressd. E-mail: lamar@chem.ucdavis.edu. Phone: (530) 752-0958. Fax: (530) 752-8995.

[1]Abbreviations: DSS, 2,2-dimethyl-2-silapentane-5-sulfonate; PH, protohemin; DMDH, 2,4-dimethyldeuterohemin; HO, heme oxygenase, hHO, human heme oxygenase 1; D140A-hHO, Asp140 → Ala human heme oxygenase 1; *Nm*HO, *Neisseria meningitidis* heme oxygenase; *Cd*HO, *Corynebacterium diphtheriae* heme oxygenase; *Pa*HO, *Pseudomonas aeruginosa* heme oxygenase; NOESY, two-dimensional nuclear Overhauser spectroscopy; TOCSY, two-dimensional total correlation spectroscopy.

Published on Web 10/20/2009

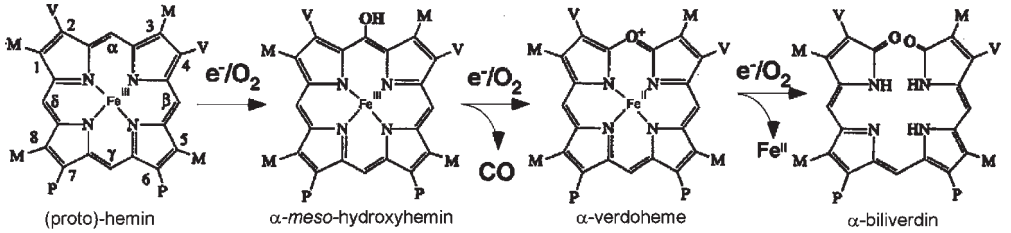

FIGURE 1: Intermediates in the catabolism of protohemin by heme oxygenase.

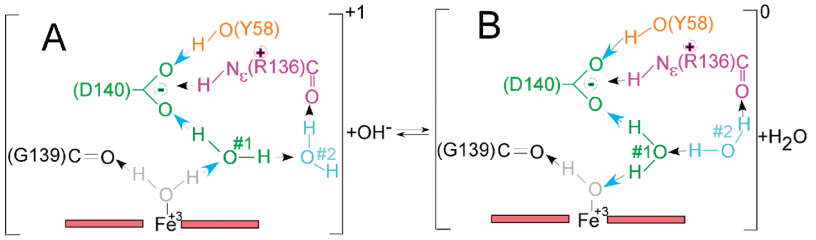

FIGURE 2: Schematic depiction of the active site of (A) hHO−DMDH−H_2O based on the crystal structure of hHO−DMDH−H_2O illustrating the position of the key residues Tyr58 (orange), Thr135 (dark blue), Arg136 (magenta), Gly139 (black), and Asp140 (pink) and the position of the ligated water molecule (gray) and two catalytically implicated nonligated water molecules #1 (green) and #2 (light blue) and (B) the expected rearrangement of H-bonds upon the deprotonation of the ligated water molecule in the hHO−DMDH−OH complex. Differences in the length of arrows depicting H-bonds in (A) and (B) reflect expected differences in H-bond strength−direction.

ordered water molecule (water molecule #1) is H-bonded to the Asp140 carboxylate, which, in turn, is also acceptor to the OH of Tyr58 and the $N_\varepsilon H$ of Arg136, as depicted schematically in Figure 2. Mutations that abolish the Asp140 carboxylate in mammalian HOs lead to formation of the inactive oxo−ferryl species (*28*, *29*), suggesting that elimination of the H-bond acceptor to the ordered water molecule #1 leads to stronger H-bond donation by water #1 to the Fe^{3+}−OOH unit, thereby accelerating heterolytic O−O bond cleavage. The HO from the pathogenic bacterium *Corynebacterium diphtheriae* (*Cd*HO) possesses (*19*) a distal H-bond network with significant sequence and structural homology to that in mammalian HOs. The homologous Asp136 → Ala mutation in *Cd*HO, however, leads (*30*) to only a ~50% inactivation, indicating that the conserved Asp carboxylate is not as crucial in modulating the H-bonding properties of the noncoordinated water molecule #1 in *Cd*HO as it is in hHO.

As an approach to understanding the differences in the distal H-bond networks among the various HOs, we have embarked on ^{1}H NMR studies of the resting state, substrate-bound complexes (*26*, *27*, *31*), which exist in an equilibrium between the high-spin aquo and, upon simple deprotonation, the low-spin hydroxo complexes, as depicted in Figure 2 for hHO. Since the reaction consists of a simple proton abstraction, it represents an ideal model for assessing the changes in the H-bond network upon converting from an H-bond donor (H_2O, Figure 2A) to an H-bond acceptor (OH^-, Figure 2B) ligand within a basically isostructural protein matrix. Information on the H-bond properties of both the exogenous ligand and members of the H-bond network is stored in the chemical shifts for these paramagnetic complexes (*32*, *33*). The paramagnetic contribution to the chemical shifts of all the nuclei of nonligated residues in both complexes arises solely from the anisotropy of the paramagnetic susceptibility tensor, χ, for which the resulting dipolar shift, δ_{dip}, in the pertinent case of axial symmetry, is given by (*32*, *33*)

$$\delta_{dip} = (12\pi\mu_0 N_A)^{-1}[\Delta\chi_{ax}(3\cos^2\theta' - 1)R^{-3}]\Gamma(\alpha,\beta,\gamma) \quad (1)$$

where, θ', Ω', and R are the proton coordinates in an iron-centered coordinate system, x', y', z', derived from crystal

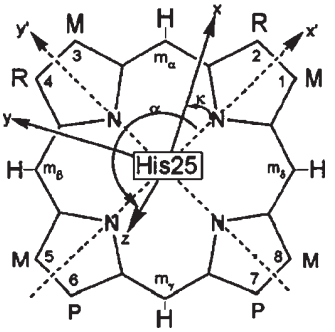

FIGURE 3: Structure of native protohemin (PH) with R = vinyl, P = propionate, and M = methyl and the 2-fold symmetric synthetic substrate, 2,4-dimethyldeuterohemin(DMDH) with R = methyl. The orientation of the magnetic axes, x, y, z, relative to the crystal-based reference coordinate system, x', y', z', is also illustrated. The angle β represents a tilt of the major magnetic axis, z, from the DMDH normal, z'; α gives the direction of the tilt as given by the angle between the projection of z on the x', y' plane and the x' axis; $\kappa \sim \alpha + \gamma$ defines the position of the rhombic axis (κ is not relevant in the pertinent case of axial magnetic anisotropy).

coordinates, $\Delta\chi_{ax}$ is the axial anisotropy of χ, and $\Gamma(\alpha,\beta,\gamma)$ is the Euler rotation matrix that transforms the reference coordinate into the magnetic coordinate system, x, y, z, when χ is diagonal. The relative orientation of the two coordinate systems is depicted in Figure 3.

The quantitation of $\Delta\chi_{ax}$ and $\Gamma(\alpha,\beta,\gamma)$, and hence δ_{dip}, is crucial for extraction of two distinct types of key structural information from the observed chemical shifts. On the one hand, δ_{dip} directly monitors the H-bond properties of the ligated water molecule/hydroxide ion (*26*, *27*, *31*, *33*). For high-spin ferrihemoproteins, $\Delta\chi$ is large, negative, and highly axial (*26*, *31*, *34*−*36*) and arises overwhelmingly from the zero-field splitting constant, D, as given by (*32*)

$$\Delta\chi_{ax} = -21g^2B^2N_AD(5k^2T^2)^{-1} \quad (2)$$

The value of D reflects the axial field strength of the ligated water molecule (*31*), which is modulated by its H-bond donor strength

to the distal residues (or ordered water molecules). For the predominantly low-spin hydroxide complex, the sign of $\Delta\chi_{ax}$ dictates (*37*) whether the lone spin is in a d_π (i.e., $(d_{xz}, d_{yz})^1$) orbital with positive $\Delta\chi_{ax}$ or in the d_{xy} orbital with characteristic negative $\Delta\chi_{ax}$, where weak H-bonding to the ligand hydroxide favors the former, while strong H-bond donation favors the latter ground state (*5*, *38*). On the other hand, the diamagnetic contribution to δ_{DSS}(obs) for labile protons can reflect on the H-bond strength. It has been demonstrated that as H-bond length decreases, the strength of the H-bond increases, and this increase results in a low-field bias of the chemical shift (*39*−*41*). In a paramagnetic system, however, the observed chemical shifts, δ_{DSS}(obs), for labile protons must be corrected for the paramagnetic contribution, δ_{dip}, to yield the diamagnetic contribution related to H-bonding, δ_{DSS}(dia*), via

$$\delta_{DSS}(\text{dia}*) = \delta_{DSS}(\text{obs}) - \delta_{dip} \quad (3)$$

In order to compare H-bond strength in two different paramagnetic derivatives, the correction for δ_{dip} must be made for each derivative. The necessary quantitative determination of $\Delta\chi_{ax}$ and $\Gamma(\alpha,\beta,\gamma)$ in eq 1 is readily achieved if sufficient experimental δ_{dip}(obs) values can be measured and a set of crystal coordinates is available to obtain R, θ', and Ω' in eq 1. Previous studies of the same complexes of *Nm*HO have shown that while both the aquo and hydroxo complexes are strongly paramagnetic (substrate methyl T_1s ~5 and 15 msec, respectively (*27*, *31*)), broadening many of the active site signals beyond detection, the necessary assignments are attainable by appropriately tailored ^{1}H 2D NMR, and the resulting quantitated δ_{dip} values allow the determination of the anisotropy and orientation of χ.

We report herein on the ^{1}H NMR properties of the aquo and hydroxo complexes of human HO#1, hHO, and the inactive point mutant (*28*) D140A-hHO. Native protohemin (PH) (R = vinyl in Figure 3) results in a static orientational heterogeneity about the α,γ-*meso* axis (*23*, *42*) that leads to loss of resolution and severely complicates resonance assignments under the diamagnetic envelope. Hence, we emphasize the synthetic, 2-fold symmetric substrate, 2,4-dimethyldeuterohemin (DMDH) (R = methyl in Figure 3) that yields a homogeneous structure essentially indistinguishable from that for the PH complex (*23*, *42*).

MATERIALS AND METHODS

Preparation of hHO. The 265-residue constructs of wild-type human heme oxygenase 1, hHO, and the Asp140 → Ala mutant, D140A-hHO, were prepared as reported previously (*7*, *28*). 2,4-Dimethylprotoporphyrin IX (Figure 3 with R = methyl) was purchased from Mid-Century Chemicals and the iron inserted by standard procedures (*43*) to yield 2,4-dimethyldeuterohemin (DMDH). The 1:1 mol equiv of DMDH or PH were titrated into an apo-hHO solution buffered at pH 6.7 with 50 mM phosphate. The substrate complexes were purified by column chromatography on Sephadex G25 and concentrated in an ultrafiltration cell to yield ~2.5 mM in WT, hHO−DMDH−H_2O, ~2.0 mM in WT hHO-PH−H_2O, and 1.5 mM in D140A-hHO−DMDH−H_2O at pH 6.7 in 50 mM phosphate. Samples in ^1H_2O were converted to ^2H_2O by column chromatography. The sample pH for reference spectra in the range of 6.7−10.3 was altered by incrementally adding 0.1 M KOH solution to the aquo complexes, 50 mM phosphate, at 30 °C. For long-term 2D NMR spectra at alkaline pH, the hydroxo sample was buffered at pH = 10.3 with 50 mM bicarbonate.

NMR Spectroscopy. ^{1}H NMR data were collected on Bruker AVANCE 500 and 600 spectrometers operating at 500 and 600 MHz, respectively. Reference spectra at 500 MHz were collected in ^1H_2O and ^2H_2O over the temperature range 10−35 °C at repetition rates of 1 s^{-1} (14 ppm bandwidth) and 5 s^{-1} (200 ppm bandwidth). Chemical shifts are referenced to 2,2-dimethyl-2-silapentane-5-sulfonate (DSS) through the water resonance calibrated at each temperature. Nonselective T_1s were estimated from the null point of a standard inversion−recovery pulse sequence. The distance of a given proton, H_i, from the iron, R_{H_i}, was estimated (*26*, *32*, *33*) from the relation $R_{H_i} = R^*_{Fe}[T_1^*/T_{1i}]^{1/6}$, using the heme methyl for H^* (R^*_{Fe} = 6.1 Å and T_1^* = 5 ms) as reference. The 600 MHz NOESY (*44*) spectra (mixing time, 40 ms) were collected over 14−20 ppm spectral width at repetition rates 1−3 s^{-1} at 20, 30, and 35 °C. The 500 MHz Clean-TOCSY (*45*) (to suppress ROESY response) spectra (spin lock 15− 40 ms) were recorded over a spectral width of 30 and 24 ppm with recycle rates of 1−3 s^{-1}, using 512 t_1 blocks of 128 or 256 scans each consisting of 2048 t_2 points. Two-dimensional data sets were processed using Bruker XWIN software on a Silicon Graphics Indigo workstation and consisted of 30° or 45° sine-squared-bell apodization in both dimensions and zero filling to 2048 × 2048 data points prior to Fourier transformation.

Magnetic Axes Determination. The anisotropy and orientation of the magnetic axes were determined (*26*, *27*, *33*, *46*) by finding the magnetic anisotropy and Euler rotation angles, $\Gamma(\alpha,\beta,\gamma)$, that rotate the crystal-structure based, iron-centered reference coordinate system, x', y', z', into the magnetic coordinate system, x, y, z, where the paramagnetic susceptibility tensor, χ, is diagonal. The angle β dictates the tilt of the major magnetic axis, z, from the heme normal z', α reflects the direction of this tilt and is defined as the angle between the projection of the z axis on the heme plane and the x' axis (Figure 3), and $\kappa \sim \alpha + \gamma$ is the angle between the projection of the x, y axes onto the heme plane and locates the rhombic axes; in the present relevant case of axial symmetry, κ is irrelevant. The magnetic axes were determined (*26*, *27*, *33*, *46*) by a least-squares search for the minimum in the error function, F/n:

$$F/n = \sum_{i=1}^{n} |\delta_{dip}(\text{obs}) - \delta_{dip}(\text{calc})|^2 \quad (4)$$

where the calculated dipolar shift in the reference coordinate system, x', y', z', (R, θ', Ω'), is given by eq 1. The observed dipolar shift for a *nonlabile proton*, δ_{dip}(obs), is given by

$$\delta_{dip}(\text{obs}) = \delta_{DSS}(\text{obs}) - \delta_{DSS}(\text{dia}) \quad (5)$$

where δ_{DSS}(obs) and δ_{DSS}(dia) are the chemical shifts, in parts per million, referenced to DSS, for the paramagnetic hHO−DMDH complexes and an isostructural diamagnetic complex, respectively. Since the assigned residues in the present ^{1}H NMR study are within a region of the hHO enzyme shown to be structurally highly conserved in the substrate and diamagnetic apo-hHO complexes (*16*, *47*), even to the strength of H-bonds (*23*, *48*), we obtain δ_{DSS}(dia), by adding the porphyrin ring current induced shift (*49*) using the crystal coordinates (*16*) of hHO−PH−H_2O, δ_{prc}, to the observed chemical shift of apo-hHO, to obtain

$$\delta_{DSS}(\text{dia}) = \delta_{DSS}(\text{apo-hHO}) + \delta_{prc} \quad (6)$$

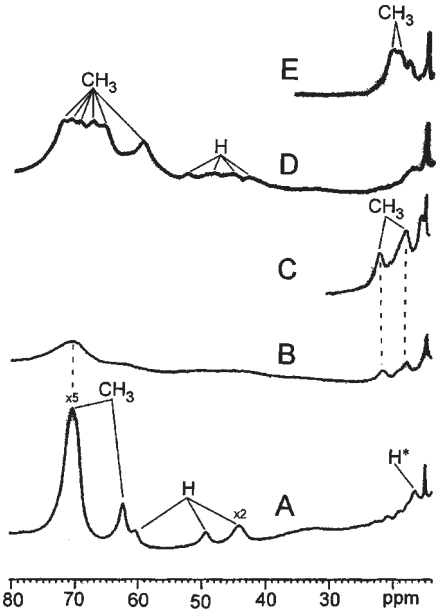

FIGURE 4: Low-field-resolved portion of the 500 MHz ^{1}H NMR spectra as a function of pH for the hHO−DMDH complexes at (A) pH 6.7, (B) pH 8.3, and (C) pH 10.3 and for the D140A-hHO−DMDH complexes at (D) pH 6.7 and (E) pH 10.3. All complexes are in ^1H_2O, 50 mM in phosphate, at 30 °C. The unassigned DMDH methyl peaks are labeled CH_3 propionate $C_\alpha H$ peaks are labeled with H, and axial His25 $C_\beta H$ is labeled H*.

RESULTS

Effect of pH on Chemical Shifts. The low-field portions of the 500 MHz ^{1}H NMR spectrum of WT hHO−DMDH complexes at pH values 6.7, 8.3, and 10.3 are illustrated in panels A, B, and C of Figure 4, respectively. The high-spin hHO−DMDH−H_2O complex dominates at low pH (Figure 4A), and the primarily low-spin hHO−DMDH−OH complex dominates at alkaline pH (Figure 4C). The extreme low-field portion in Figure 4A is typical of a high-spin complex (*26*, *31*, *33*), with only one of the six DMDH methyl peaks resolved; also observed are four low-field, single proton peaks labeled H that arise from propionate C_αHs. The methyl and single proton peaks exhibit T_1s of ∼4−5 ms, typical of other high-spin ferrihemoproteins (*33*). A fifth resolved single proton peak near 20 ppm, labeled H*, exhibits a shorter T_1 (< 3 ms) indicative of the axial His25 $C_\beta H$. On the high-field side (not shown), we detect two very strongly relaxed (T_1 < 5 ms) and severely broadened resonances at ∼−5 and ∼−7 ppm on a strongly sloping baseline, of which the latter peak appears to exhibit more intensity than for a single proton. At intermediate pH = 8.2 (Figure 4B) the intensity of the low-field peaks clearly decreases, and two new strongly relaxed and broadened signals appear at ∼16 and ∼22 ppm, which dominate the spectrum at pH 10.3 (Figure 4C). The strongly hyperfine shifted DMDH signals exhibit slow exchange (*50*) in the acid−alkaline transition. The two resolved and strongly relaxed (T_1 ∼15 ms) signals labeled CH_3 in Figure 4C have intensity 3 relative to other assigned single protons, exhibit the same T_1 as the assigned methyls in *Nm*HO−PH−OH (*27*), and hence can be attributed to two of the six DMDH methyls in the low-spin hydroxide complex.

Some of the weakly to inconsequentially relaxed labile proton peaks in the spectral window 10−17 ppm for both the DMDH (not shown; see Supporting Information Figure S1) and PH (not shown) complexes also exhibit significant chemical shift difference at pH 6.7 and 10.3. These signals do not change intensity but rather change chemical shifts with pH consistent with fast proton exchange on the NMR time scale (*50*). A plot of the chemical shift versus pH for the resolved low-field labile proton signals of wild-type hHO−DMDH complexes is reproduced in Figure 5, for which the inflection point is near pH ∼8.5. It is noted that the signal for Tyr58 $O_\eta H$ actually broadens, as well as changes shift, as pH is raised, disappears near pH ∼8, but reappears at pH ∼9 near 15.5 ppm and further narrows at pH 10.3. A similar plot for the WT hHO−PH complex reveals an inflection point near pH ∼8.0 (not shown).

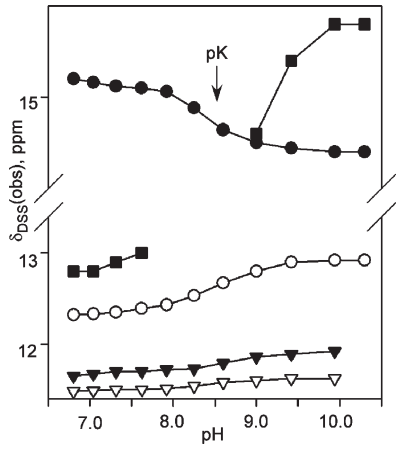

FIGURE 5: The Henderson−Hasselbalch plot of δ_{DSS}(obs) versus pH for low-field-assigned labile proton peaks in the hHO−DMDH-complex in ^1H_2O, 50 mM in phosphate, at 30 °C. The apparent p*K* is ∼8.5, indicated by vertical arrows. The assigned residues are Tyr58 $O_\eta H$ (closed square), His132 $N_\varepsilon H$ (closed circle), Arg85 NH (open circle), Ala165 NH (closed triangle), and Trp96 $N_\varepsilon H$ (open triangles).

The mutant complex exhibits resolved and relaxed DMDH resonances at low pH (Figure 4D) and at high pH (Figure 4E) similar to those of the same WT complex in panels A and C of Figure 4, respectively, except that the mutant resonances are a factor ∼2−5 broader than in the WT complexes, in spite of unchanged T_1s. The much larger line widths at both pH extremes in the mutant are also observed for the inconsequentially relaxed, resolved labile proton signals in the 15−10 ppm spectral window (not shown; see Supporting Information Figure S1). At intermediate pH values, the low-field methyl peaks in Figure 4D lose intensity, and the labile protons in the 15−10 ppm window change chemical shifts in the same manner as for the WT complex described above. An apparent inflection point for the lowest field labile proton resonance occurs near pH ∼8.5 (not shown).

Assignment Protocols. We target two classes of residues in this study: those that possess labile protons that are significantly low-field shifted by H-bonding (i.e., shifted to low field of 9 ppm) and those that exhibit significant δ_{dip}. The former involves residues with R_{Fe} > 10 Å and are assigned sequence-specifically via standard backbone N_i−N_{i+1}, α_i−N_{i+1}, β_i−N_{i+1}, ... connections (*51*) and TOCSY characterization of side chains, as reported in detail previously (*23*, *48*) for both hHO−DMDH−CN and apo-hHO. For the latter residues, a more indirect, albeit equally effective, route to assignments is necessary. Strong paramagnetic relaxation precludes assignment of residues in the active site unless their signals are well resolved outside the intense diamagnetic envelope (*26*, *27*). However, since δ_{dip} depends more weakly on R_{Fe} ($\propto R_{Fe}^{-3}$) than relaxation ($\propto R_{Fe}^{-6}$), the residues in the shell R_{Fe} ∼10−15 Å (T_1 > ∼80 ms) are expected to be readily assignable and still exhibit sufficiently large

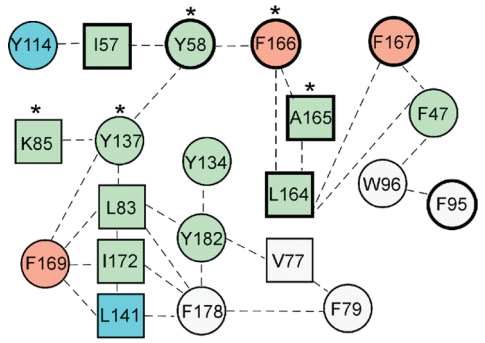

FIGURE 6: Schematic depiction of the interresidue contacts predicted by the crystal structure of hHO−PH−H_2O and observed herein by NMR in hHO−DMDH−H_2O and, in part, in hHO−DMDH−OH. The NMR established connectivities rely on NOESY connection over a range of temperatures among characteristic TOCSY-detected spin systems for residues with variable magnitude dipolar shift. Circles and squares reflect aromatic and aliphatic residues, and the colors reflect the observed (and subsequently correctly predicted) magnitude of the largest dipolar shifts for the residues; $|\delta_{dip}| \geq 1.0$ (pink), 0.5 ppm $< |\delta_{dip}| < 1.0$ ppm (blue), and $0.2 < |\delta_{dip}| < 0.5$ ppm; residues with the $|\delta_{dip}| < 0.2$ ppm are shown in gray. Residues with labile protons involved in relatively strong H-bonds are marked by an asterisk, and residues whose assignment can be established sequence-specifically are shown in bold.

δ_{dip} to quantitate the magnetic axes. We note that in this study we have no need to establish molecular structural details; these are provided directly by the hHO−DMDH−H_2O crystal structure (*16*). Rather, our interests focus entirely on the electronic structure and magnetic properties of the chromophore, and hence the crystallographic data are freely utilized to make the necessary assignments of the dipolar-shifted residues required to quantitate the magnetic axes. Hence, we emphasize dipolar contacts among TOCSY-detected spin systems that are predicted by the crystal structure. Variable temperature serves as an effective "third dimension" that guarantees the uniqueness of both scalar and dipolar contacts.

Of particular interest in this study are the dipolar-shifted aromatic rings and some of their key aliphatic contacts with upfield, resolved methyls of aliphatic side chains in a remarkably extensive aromatic cluster (*16*, *47*) with the predicted (and observed; see below) contacts schematically depicted in Figure 6. The residues are color shaded to reflect the relative magnitude of expected δ_{dip}. Aromatic rings are much more readily assigned than aliphatic side chains because of the much less crowded aromatic (particularly in ^2H_2O) than aliphatic spectral window. The rings and aliphatic residue termini are readily characterized in TOCSY spectra in WT complexes (not shown; seeSupporting Information Figures S2, S3, and S4) and exhibit ring labile proton, ring-aliphatic, and interaromatic ring NOESY contacts of which key portions are depicted in Figures 7, 8, and 10 (and Supporting Information Figures S5 and S6).

Helical Assignments in WT hHO−DMDH−H_2O. Sequential backbone assignments, as were found to be the case in the low-spin cyanide complex (*23*) and diamagnetic apo-hHO (*24*), are restricted to helical fragments where at least one of the member peptide NHs is resolved due to a sizable low-field bias from H-bonding (His84-Lys86 and Leu164-Phe167) or where peptide exchange is so slow so as to allow detection of N_i-N_{i+1} connections in ^2H_2O (Ile57-Ala60 and Leu93-Trp96). These four fragments are similarly assigned here for hHO−DMDH−H_2O. The key contacts for Leu164-Phe167 are shown in Figure 7A,B. For this fragment, only the $C_\alpha H$ of

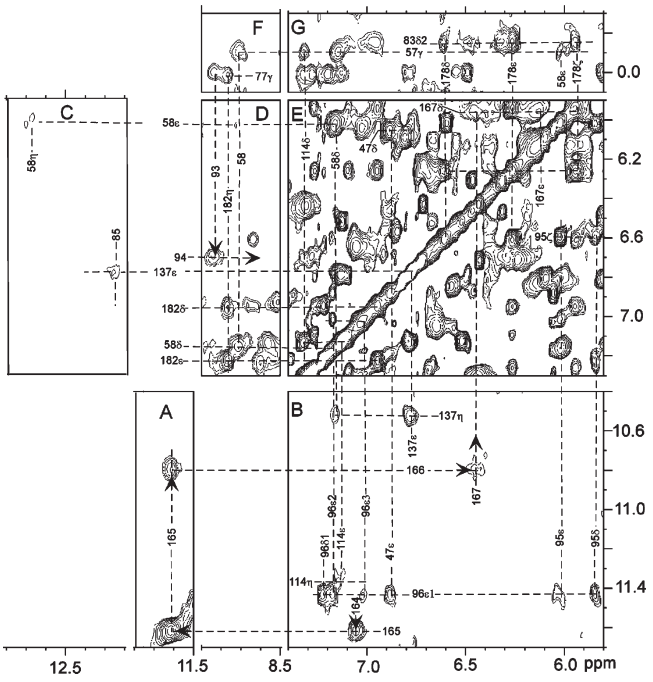

FIGURE 7: Portions of the 600 MHz ^1H NMR NOESY spectrum (spectral width 38 ppm, repetition rate 2 s^{-1}, mixing time 40 ms) of hHO−DMDH−H_2O in ^1H_2O, 50 mM in phosphate, at pH 6.7 and 30 °C illustrating key contacts to labile protons involved in strong H-bonds. The sequential N_i-N_{i+1} connections for Leu164-Phe167 (A, B, C) and Leu93-Ala94 (D) are shown by arrows. The key Ile57 $C_\gamma H$ contact to the NH of Tyr58 and the ring of Tyr114 is shown in (D); the expected Tyr58 to Tyr137 contact is found in (E). The key Arg85 NH to Tyr137 ring (C) and the identification of the $O_\eta Hs$ signals for Tyr114 and Tyr137 are shown in (B).

Leu164 and both $C_\alpha H$ and $C_\beta H$ of Ala165 are identified by TOCSY. The ring $C_\delta Hs$ of both Phe166 and Phe167 are expected to exhibit strong NOESY cross-peaks to their respective peptide NHs. Such a cross-peak is observed in Figure 7E for Phe167, but the same cross-peak for Phe166 could not be detected. The failure to detect the Phe166 NH to $C_\delta H$ NOESY cross-peak is attributed to the $C_\delta H$ resonating under the residual solvent signal; the predicted δ_{dip} for this proton (see below) is consistent with this conclusion.

Aromatic Cluster in WT hHO−DMDH−H_2O. TOCSY spectra reveal (not shown; see Supporting Information Figures S2 and S3) the rings of seven Phe (47, 79, 95, 166, 167, 169, 178), five Tyr (58, 107, 114, 137, 182), and two Trp (96, 101) and the termini of three Leu (83, 93, and 141), two Ile (57, 172), two Val (59, 77), and four Ala (60, 94, 110, 165) which exhibit sufficient upfield ring currents and/or δ_{dip} to provide excellent spectral resolution on the high-field side of the aliphatic envelope. Inspection of the aromatic cluster depicted in Figure 6 reveals that the above sequence-specific assignments provide the following key entry points into the aromatic cluster, Ile57, Tyr 58, Arg85, Leu164, Ala165, and Phe167; these residues are shown in bold in Figure 6. NOESY spectra in ^1H_2O identify the inter-ring contacts of Trp96 to both Phe47 and Phe195 (Figure 7B) and Tyr137 ring contact to Arg85 NH (Figure 7C). The NOESY connections (Figure 7E) between a TOCSY-detected (not shown; see Supporting Information Figure S4) aromatic ring and the peptide NH for residue 58 (Figure 7D) identify the Tyr58 ring. The NOESY contact of the Tyr58 ring $C_\varepsilon H$ to the strongly low-field-shifted, broad, but only very weakly relaxed labile proton at 12.8 ppm (Figure 7C) locates the key Tyr58 $O_\eta H$.

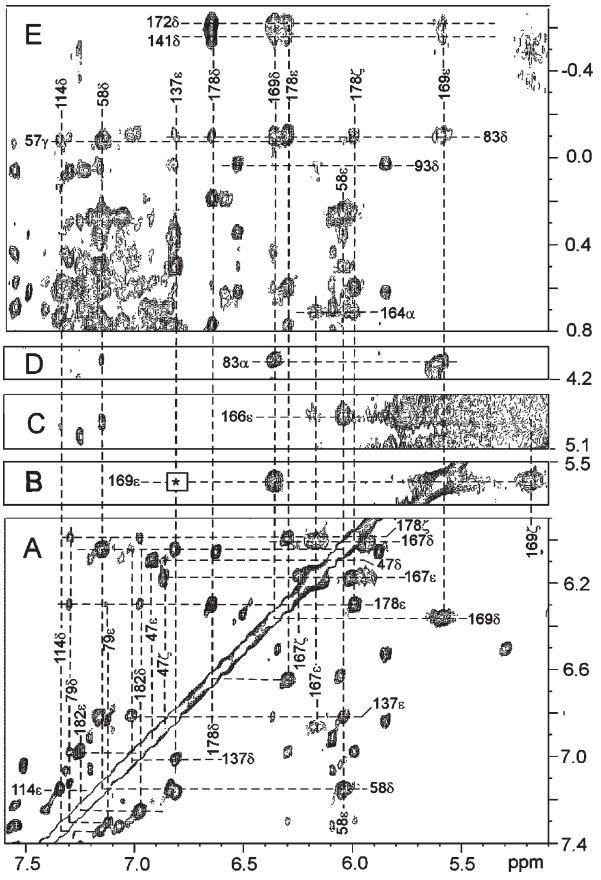

FIGURE 8: Portions of the 600 MHz ^{1}H NMR NOESY spectrum (spectral width 22 ppm, repetition rate 1.5 s^{-1}, mixing time 40 ms) of hHO−DMDH−H_2O in ^2H_2O, 50 mM in phosphate, at pH 6.7 and 35 °C illustrating key interaromatic contacts (A, B, C) and aromatic−aliphatic (D, E) contacts. (A) Phe47-Phe167, Phe95-Trp96, Tyr58-Tyr137, Phe79-Phe178, and Phe178-Tyr182, (B) Tyr137-Phe169, (shown by box where cross-peak is observed in lower contours), (C) Phe166-Tyr58 and Phe166-Phe167, and aromatic−aliphatic contacts (D) Phe169-Leu83; (E) Leu164 C_αH-Phe167, Ile57-Tyr114, and Leu83, Leu141, and Ile172 contacts to the rings of both Phe169 and Phe178.

The remaining contacts in Figure 6 are optimally detected in ^2H_2O solution. The key interactions among the strongly dipolar shifted aromatic rings of Phe47, Tyr58, Tyr177, Phe166, Phe167, and Phe169 are illustrated in Figure 8A−C. Two characteristically strong interresidue ring−C_αH contacts involving Tyr169/Leu83 and Phe167/Leu164 are shown in panels D and E of Figure 8, respectively. For residues with sufficiently large δ_{dip} to use in determining the magnetic axes (shaded in pink, green, or blue in Figure 6), at least two independent sequences of contacts with different residues, over a range of temperature, are observed to confirm their assignments. The contacts involving the more weakly shifted rings of Phe79/Tyr182/Phe178 are included in Figure 8A. The key links of the Phe169 and Phe178 rings to the side chains of Leu83, Leu141, and Ile172 are shown in Figure 8E. The Tyr134 C_αH is readily detected by the predicted very strong NOESY cross-peak to the ring of Tyr182, and the C_αH also exhibits the expected NOESY cross-peak to the Tyr134 C_δH (not shown). The expected interactions among the aliphatic termini are similarly observed in NOESY spectra (not shown; see Supporting Information Figure S5). The detected interresidue cross-peaks for the assigned residues in the aromatic cluster completely conform to those predicted by the crystal structure (*16*, *47*) as shown in Figure 6. Lastly, the strongly low field shifted ring labile protons of Tyr114 and Tyr137 (Figure 7B) to the respective rings are readily detected in H_2O. The chemical shifts for key residues in the aromatic cluster with significant δ_{dip} are listed in Table 1; the remaining data are provided in Supporting Information (Table S1).

Table 1: Chemical Shift Data for Assigned Strongly Dipolar Shifted Residues for the Aquo and Hydroxo Complexes of Human Heme Oxygenase with 2,4-Dimethyldeuteroheme

			hHO−DMDH−X	
residue	proton	δ_{DSS} (dia)[a]	δ_{DSS} (obs),[b] X = H_2O	δ_{DSS} (obs),[c] X = OH^-
Phe47	C_δHs	6.16	6.06	6.04
	C_εHs	7.05	6.89	7.13
	C_ζH	7.09	6.80	7.24
Tyr58	C_δH	7.13	7.15	7.53
	C_εH	6.36	6.01	6.60
Leu83	C_αH	4.43	4.08	4.52
	C_γH	1.10	0.97	1.20
	$C_{\delta1}H_3$	0.72	0.55	0.74
	$C_{\delta2}H_3$	0.18	−0.16	0.30
Tyr114	C_δHs	6.98	7.32	6.96
	C_εHs	6.641	7.13	6.66
Tyr134	C_δHs	7.47	8.40	
	C_εHs	7.29	8.52	
Tyr137	C_δHs	7.30	7.12	7.52
	C_εHs	6.93	6.79	7.03
Phe166	C_δHs	5.45	4.7 ± 0.2	5.35
	C_εHs	6.19	4.89	5.92
	C_ζH	7.00	5.71	7.15
Phe167	C_δHs	7.07	5.97	7.26
	C_εHs	7.31	6.13	7.47
	C_ζH	7.01	6.1 ± 0.2	7.17
Phe169	C_αH	3.81	3.20	
	$C_{\beta1}$H	2.55	2.06	
	$C_{\beta2}$H	2.37	2.02	
	C_δHs	6.95	6.32	7.11
	C_εHs	6.58	5.55	
	C_ζH	6.6 ± 0.1	5.17	
Ile172	C_αH	3.78	3.67	
	C_βH	1.44	1.18	1.50
	$C_{\gamma1}$H	−0.12	−0.32	0.00
	$C_{\gamma2}$H	0.93	0.70	0.97
	$C_\gamma H_3$	0.28	0.15	0.39
	$C_\delta H_3$	−0.47	−0.68	−0.28
Tyr182	C_δHs	6.69	6.95	6.71
	C_εHs	6.95	7.22	7.02

[a]Chemical shift in ppm at 30 °C in ^1H_2O, 100 mM in phosphate, pH 7.4, referenced to DSS through the water signal, obtained via eq 5. [b]Chemical shift in ppm at 30 °C in ^1H_2O, 50 mM in phosphate, pH 6.7, referenced to DSS through the water signal. [c]Chemical shift in ppm at 30 °C in ^1H_2O, 50 mM in carbonate, pH 10.3, referenced to DSS through the water signal.

Magnetic Axes for WT hHO−DMDH−H_2O. The relatively small δ_{dip} for assigned residues with R_{Fe} > 10 Å requires the use of δ_{DSS}(dia) for an actual isostructural diamagnetic complex, rather than the more approximate calculated chemical shifts (*52*) based on the crystal structure. Fortunately, the aromatic cluster of hHO resides in a portion of the molecular structure that exhibits completely conserved structure in diamagnetic apo-hHO (*47*, *48*) and any substrate complex (*16*, *23*), right down to conserved H-bond strength for a labile proton within the cluster (NH to Arg85, Ala110, Ala165, and Phe166 and OHs of Tyr114 and Tyr137). Since the Tyr58 OH chemical shift exhibits strongly variable low-field bias, and hence variable H-bonding, in apo-HO and its various ligated substrate complexes (*23*, *48*), this residue and its closest contacts, Ile57 and Phe166, were excluded

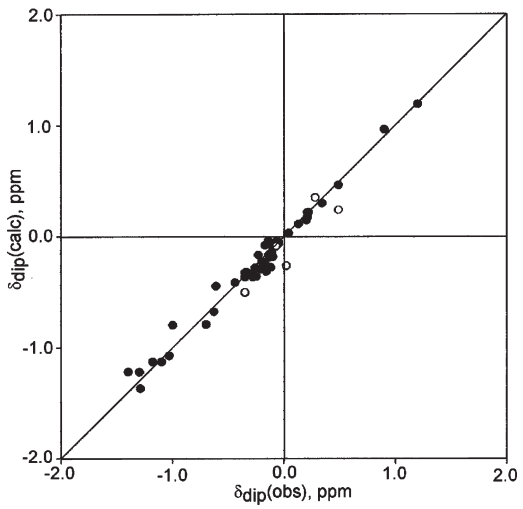

FIGURE 9: Plot of δ_{dip}(obs) (obtained via eq 5) versus δ_{dip}(calc) (obtained via eq 1) for the optimized magnetic axes/magnetic anisotropy obtained for hHO−DMDH−H_2O at pH 6.7 and 30 °C by a three-parameter search for $\Delta\chi_{ax}$, α (tilt direction), and β (tilt from heme normal), with $\Delta\chi_{ax} = -2.56 \times 10^{-8}$ m^3/mol, α = 183°, and β = 3°, where the axial anisotropy lines up with the Fe−N_ε (His25) vector. The closed circles represent the input data, and open circles represent noninput data (i.e., Tyr58).

as input to the magnetic axes determination. The δ_{DSS}(dia) values obtained via eq 6 are given in Table 1 (and Supporting Information Table S1). Assuming an axial χ oriented normal to the heme (β = 0), a one parameter ($\Delta\chi_{ax}$) search yielded $\Delta\chi_{ax} = -2.55 \pm 0.06 \times 10^{-8}$ m^3/mol and a reasonably low residual error function, F/n = 0.47 ppm^2. Extension to a three-parameter (α, β, $\Delta\chi_{ax}$) search that allows for variable orientation of the axial χ tensor relative to the heme plane leads to α = 183 ± 30°, β = 3 ± 1°, and $\Delta\chi_{ax} = -2.56 \pm 0.05 \times 10^{-8}$ m^3/mol and (via eq 2) D = 9.6 ± 0.2 cm^{-1}, a significantly reduced residual error function, F/n = 0.29 ppm^2, and an excellent correlation between δ_{dip}(obs) and δ_{dip}(calc) as depicted in Figure 9; $\Delta\chi_{ax}$ appears to be oriented along the His25 N_δ−Fe bond. The δ_{dip}(calc) for all assigned residues, as well as for strongly relaxed proximal and distal helical residues with potentially sufficiently large δ_{dip} to yield resolved signals, are listed in Supporting Information.

Assignments in WT hHO−DMDH−OH. The sequential N_i−N_{i+1} connections for Ile57-Ala60, His84-Lys86, Leu93-Trp96, and Leu164-Phe167 could be observed even at pH 10.3, with chemical shift similar to those for hHO−DMDH−H_2O. Key NOESY contacts are depicted in Figure 10, while TOCSY data and additional NOESY data are provided in Supporting Information Figures S4 and S6. A NOESY contact of an aromatic ring to the backbone of the peptide NH for residue 58 locates the Tyr58 ring (not shown; see Supporting Information Figure S6). The ring C_εH, moreover, exhibits a NOESY cross-peak to the extreme low-field, broad, labile proton signal, as shown in Figure 10C, and confirms the important Tyr58 O_ηH assignment inferred from the pH titration in Figure 5. The Arg85-Lys86 backbones are identified by their characteristic contacts and the significant low-field bias of the former NH and the expected Arg85 NH contact to the rings of both Tyr58 and Tyr137 (Figure 10D). Similarly, the three-spin ring contact to the sequence-specifically assigned NHs of Phe166 and Phe167 provides the ring assignments.

Tyr58, Phe95, Phe166, and Phe167 provide key entry points to the aromatic cluster in Figure 6. TOCSY spectra (not shown; see

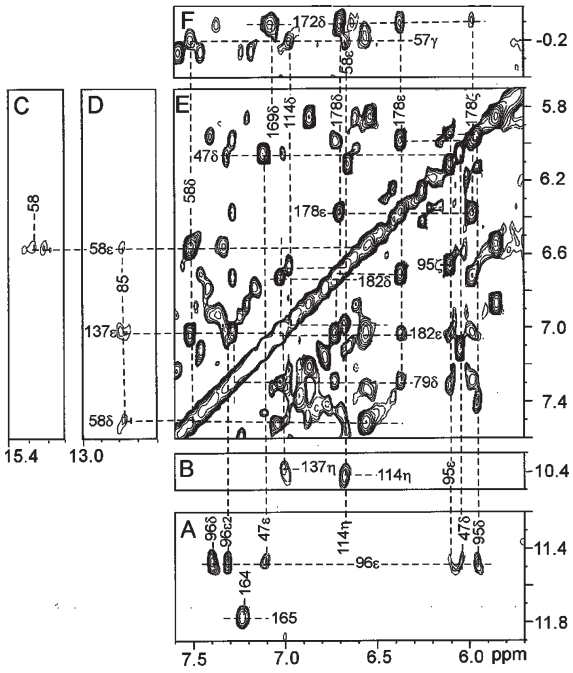

FIGURE 10: Portion of the 600 MHz ^{1}H NMR NOESY spectrum (spectral width 20 ppm, repetition rate 1.5 s^{-1}, mixing time 40 ms) for hHO−DMDH−OH in ^1H_2O, 50 mM in bicarbonate, at 30 °C, pH 10.3, illustrating key interresidue contacts for labile protons involved in relatively strong H-bonds (A, B, C), interaromatic ring contacts (A, E), and aliphatic−aromatic contacts (F) where the aromatic cluster is depicted in Figure 6. Noteworthy is the broad cross-peak between a broad extreme low-field labile proton peak with the Tyr ring C_εH that identifies the Tyr58 O_ηH. Further relevant spectra are provided in Supporting Information Figure S6.

Supporting Information Figure S4) locate additional aromatic rings and the termini of two Iles and one Leu that exhibit (Figure 10) among themselves the contacts predicted for the aromatic cluster as depicted in Figure 6. This locates all of the key residues in Figure 6 except for Tyr134 and Leu141. A TOCSY peak for the Phe169 ring could not be observed, but the predicted strong NOESY contact of the Ile172 $C_\delta H_3$ to an aromatic proton at 7.1 ppm (Figure 10F) identifies the Phe169 C_δH; the C_εH shift must be too close (±0.2 ppm) to resolve from the diagonal. Contacts of low-field-shifted labile protons to the Tyr114 and Tyr137 C_εHs (Figure 10B) locate their O_ηHs. The chemical shifts for key residues in the aromatic cluster are listed in Table 1; other data are provided in Supporting Information (Table S1).

Magnetic Axes of WT hHO−DMDH−OH. Inspection of the data in Table 1 reveals that the diamagnetic δ_{DSS}(dia) for residues with significant δ_{dip} generally lies between the δ_{DSS}(obs) for the hHO−DMDH−H_2O and hHO−DMDH−OH complex or that δ_{dip} is necessarily of opposite sign in the two complexes and of much smaller magnitude in the latter complex. Depending on the selection of input δ_{dip} three-parameter searches lead to $\Delta\chi_{ax}$ variable over the range (0.4−0.8) × 10^{-8} m^3/mol and with small to moderate tilts (β) < 15° of the major axis; it is noted that $\Delta\chi_{ax}$ is always positive. A reasonable set of input data yields $\Delta\chi_{ax} = (0.7 \pm 0.1) \times 10^{-8}$ m^3/mol, β = 15 ± 4°, and α = 240 ± 30°. The generally poorer fit of δ_{dip}(obs) vs δ_{dip}(calc) for the hydroxo (not shown; see Supporting Information Figure S7) than the aquo complex (Figure 9) is likely due to the different pHs of the δ_{dip}(dia) and δ_{dip}(obs) for the hydroxo complex and its much smaller anisotropy that results in larger uncertainties in δ_{dip}. Nevertheless, the important conclusion is that $\Delta\chi_{ax}$ is positive, as

in low-spin hHO−DMDH−CN, but considerably smaller and $\delta_{dip} < 0.1$ ppm for all labile protons of interest except the Tyr58 OH, where it is ~0.4 ppm.

Resonance Assignments in D140A-hHO−DMDH Complexes. The greater line widths for all resonances for the D140A-hHO than the WT complexes at both pH extremes (Figure 4D,E and Supporting Information Figure S1) preclude detection of any useful TOCSY cross-peaks and allowed only very limited differentiation of intra- from inter-ring NOESY contacts (data not shown). Only the labile proton peaks resolved on the low-field side of the diamagnetic envelope could be assigned, based solely on the similarity of their NOESY cross-peak pattern to those observed for the WT complexes. This provided assignments for several peptide H-bonds (Arg85, Ala110, Ala165, Phe166) and two side chain N_εs (Trp96, His132) in both the aquo and hydroxo complexes. These data are given in Supporting Information (Table S1). In particular, we were unable to locate any dipolar-shifted aromatic rings that would allow an estimate of the magnetic anisotropies of either complex, and could find no evidence for a low-field labile proton that could arise from the Tyr58 OH in either complex.

DISCUSSION

Acid ↔ Alkaline Transition. The p*K* for hHO−PH−H_2O has been reported as ~8.0 (*53*). The inflection in the plot of chemical shift vs pH for the low-field signals for the hHO−PH complexes occurs at pH ~8.0 (data not shown), confirming the correlation between the optically detected (*53*) and the presently ^{1}H NMR-detected acid ↔ alkaline transition. The chemical shift changes with pH for the WT DMDH complex (Figure 5) correlate with the intensity loss of the high-spin aquo complex peaks and exhibit inflection points at pH ~8.5. The ~0.5 unit elevation of the p*K* with DMDH over that with PH is consistent with the stronger basicity of the former substrate; a similar ~0.5 unit elevation of the p*K* upon replacing vinyl by alkyl groups has been observed with globins (*54*).

The rate of the acid−alkaline interconversion for WT hHO complexes is much faster than that reported for the *Nm*HO−PH−H_2O/OH complexes (*27*). The slow exchange limit for DMDH methyls in hHO−DMDH−H_2O dictate (*50*) (chemical shift difference ~60 ppm at 500 MHz) that the exchange lifetime $\tau > \sim 10\ \mu$s, while the fast exchange limit for the Tyr58 OH peak (chemical shift difference 2.58 ppm at 600 MHz) dictates that $\tau < 100\ \mu$s. An estimate of the excess line width for the DMDH methyl composite peak at 66 ppm at the p*K* yields $\tau \sim 40\ \mu$s. For the *Nm*HO−PH−H_2O/OH complexes all signals were in the slow-exchange limit, and the degree of saturation transfer (*27*, *50*) near the p*K* indicates $\tau \sim 50$ ms in *Nm*HO, some ~10^3 longer than in hHO. The more rapid proton transfer in hHO than *Nm*HO may arise from the larger water-filled cavities in the former (*16*, *18*) which would make the exogenous ligand more susceptible to OH^- attack. Preliminary results[2] indicate that the acid−alkaline transition for *Cd*HO−DMDH complexes (*19*) occurs at a rate comparable to that in hHO, with the substrate methyls in slow exchange and all amino acid signals in fast exchange.

Electronic/Magnetic Properties of WT hHO−DMDH−H_2O. The low-field, resolved portion of the ^{1}H NMR spectrum of hHO−DMDH−H_2O resembles that of a typical six-coordinate high-spin ferrihemoprotein (*33*), with substrate methyl T_1s ~4−5 ms. The pattern of the substrate methyl shifts has been proposed to reflect the orientation of the axial His imidazole (*55*). However, the centrosymmetric DMDH yields five essentially degenerate methyl peaks. Hence the axial His orientation is not reflected in the methyl contact shift pattern. While the methyl T_1s of 4−5 ms for hHO−DMDH−H_2O are the same (*26*) as those in *Nm*HO−PH−H_2O, the line widths in the former complex are significantly greater than for the latter complex, in part because hHO is 25% larger (265 aa) than *Nm*HO (210 aa), which results in both the normal increase in line width expected with size and an increase in the Curie relaxation (*32*, *33*). This increased line width made it much more difficult to detect strongly relaxed peaks resolved from the intense diamagnetic envelope. The value of *D* for the hHO−DMDH−H_2O complex (9.6 cm^{-1}) is slightly smaller than the value reported for the *Nm*HO−DMDH−H_2O complex (*31*) (9.8 cm^{-1}), but not outside experimental uncertainty.

Only two signals can be detected outside the 10 to −4 ppm spectral window that do not arise from the heme. They resonate upfield and are very broad and strongly relaxed and are detected on a very strongly sloping baseline, with an apparent single proton peak at ~−5 ppm and a strongly relaxed composite/methyl signal near ~−8 ppm. Inspection of predicted δ_{dip} (not shown; see Supporting Information Table S1) reveals that the following signals could be expected to appear upfield of ~−2.0 ppm: His25 $C_\alpha H$ (−6.6 ppm, T_1 <4 ms), Glu29 $C_{\gamma 1}H$ (−4 ppm, T_1 <2 ms), Asp140 $C_\alpha H$ (−7 ppm, T_1 ~5 ms), Gly143 NH (−15 ppm, T_1 <1 ms), Gly143 $C_{\alpha 1}H$ (−17 ppm, T_1 <1 ms), and Leu147 $C_{\delta 1}H_3$ (−7 ppm, T_1 ~4 ms). The His25, Glu29, and both Gly143 signals would be much too broad to detect on the sloping baseline; the Asp140 $C_\alpha H$ and Leu147 $C_{\delta 1}H_3$ shift/relaxation properties are consistent with the broad single proton peak at −5 and the more intense peak centered at −7.

The value for $\Delta\chi_{ax}$ could not be determined for D140A-hHO−DMDH−H_2O. However, the similarity in chemical shifts to the WT complex (Supporting Information Table S1) for those residues which could be assigned in the mutant suggests a similar $\Delta\chi_{ax}$.

Electronic/Magnetic Properties of WT hHO−DMDH−OH. The low-field DMDH methyls near 20 ppm with T_1 ~15 ms are similar to those in other low-spin hydroxy ferrihemoproteins, (*33*) in particular to those for *Nm*HO−PH−OH (*27*). The uncertainty in the determined $\Delta\chi_{ax}$ is much larger (fractionally) than for hHO−DMDH−H_2O. This results from much smaller δ_{dip}(obs) (by a factor ~4 smaller) than in the aquo complex. However, as evidenced most clearly by the residues with the largest δ_{dip} in hHO−DMDH−H_2O, the $\Delta\chi_{ax}$ for hHO−DMDH−OH is clearly positive, as found (*23*) for hHO−DMDH−CN, but numerically much smaller than in either the high-spin aquo or low-spin cyano complexes. The alternate $S = {}^1/_2$ orbital ground states, $d_\pi (d_{xz}, d_{yz})^1$ and $d_{xy} (d_{xy})^1$, exhibit (*37*) characteristically opposite signs for the $\Delta\chi_{ax}$, with the former $\Delta\chi_{ax} > 0$ and the latter necessarily with $\Delta\chi_{ax} < 0$. The presently estimated $\Delta\chi_{ax} = (0.7 \pm 0.1) \times 10^8$ m^3/mol is clearly positive, dictating a conventional d_π ground state. The same conclusion based on the same type of data has been reached (*27*) for *Nm*HO−PH−OH. The d_π, rather than d_{xy}, ground state is further supported by the substrate methyl hyperfine shift patterns. The hHO−DMDH−OH methyl shift pattern exhibits significant asymmetry with two signals strongly low-field shifted

[2] See www.bmrb.wisc.edu.

and the other four methyls with much smaller contact shifts left unresolved under the diamagnetic envelope, just as observed (*23*) for hHO−DMDH−CN^-. The d_{xy} ground state does not lead to significant hyperfine shifts for substrate methyls (*37*) and has no basis for inducing asymmetry among such shifts.

The value for $\Delta\chi_{ax}$ could not be determined for D140A-hHO−DMDH−OH. However, the similarity in chemical shifts to the WT complex for those residues which could be assigned (Supporting Information Table S1) suggests a similar $\Delta\chi_{ax}$, and hence a d_π ground state, for the mutant hydroxo complex.

H-Bonding Properties of the Exogenous Ligand. The value of $D = 9.6\ cm^{-1}$ for WT hHO−DMDH−H_2O is numerically smaller (although within experimental uncertainty) than for *Nm*HO−DMDH−H_2O (*31*) ($D = 9.8\ cm^{-1}$), indicating that the axial field strength may be somewhat stronger in the hHO than *Nm*HO complex, inasmuch as *D* depends inversely on axial field strength (*31*, *56*). Since the axial field strength of ligated water increases with increased H-bond donation by the ligated water to a distal residue (or ordered water molecule), the present data suggest that H-bonding by the ligated water to the nonligated water #1 (see Figure 2) is slightly stronger in hHO than *Nm*HO. However, the distal H-bond networks for these two HOs differ substantially (*16*, *18*) in terms of the number of distal residues interacting with the ordered water molecules. A much more informative comparison would be between hHO and the *Cd*HO complexes (*19*, *24*) for which both the distal H-bonding network and the aromatic cluster are very similar (*vide infra*).

The ligated hydroxide is generally a strong-field ligand and is expected to serve as an H-bond acceptor to the nonligated water molecule #1 (Figure 2B). For weak to moderate H-bond donation to the ligated OH^-, the d_π, $S = {}^1/_2$ ground state is expected and is indeed observed for hydroxo complexes (*33*, *37*). In the case of very strong distal H-bonding to the ligated hydroxide, the axial field strength could be sufficiently weakened so as to stabilize the d_{xy}, $S = 1/2$ ground state (*37*, *38*). Such H-bonding, and a d_{xy}, $S = {}^1/_2$ ground state, has been proposed (*5*, *38*) for *Pa*HO−PH−OH^-. Our findings of $\Delta\chi_{ax} > 0$ for both the present hHO and the previously reported (*27*) *Nm*HO hydroxo complexes argue against such strong H-bonding to the ligated hydroxide in either the hHO or *Nm*HO complex.

Effect of Ligand Deprotonation on the H-Bond Network. Assigned labile protons that exhibit either a significant difference (> 0.2 ppm) in δ_{DSS}(obs) between the aquo and hydroxo complex or exhibit significant low-field shifts due to H-bonding (δ_{DSS}(obs) to the low field of 9 ppm) are listed in Table 2. Using the $\Delta\chi_{ax}$ and α,β values determined above for the WT complexes, δ_{DSS}(dia*) for each complex was obtained using eqs 5 and 3, and the results are listed in Table 2. For hHO−DMDH−OH, δ_{dip}(calc) for all labile protons of interest (except Tyr58 OH) is $< |0.1|$ ppm, such that the uncertainties in δ_{DSS}(dia*) are $< |0.1|$ ppm. For Tyr58 OH, δ_{dip}(calc) is 0.4 ppm, and the range of parameters indicate that uncertainty of ±0.2 ppm. In the case of hHO−DMDH−H_2O, the magnetic axes are considerably better defined than for the hydroxide compound, and the range of parameters indicate uncertainties of 10% in δ_{dip}(calc), which translates into uncertainties ±0.1 ppm for all assigned labile protons except Tyr58 OH, where the uncertainty is ±0.2 ppm. Hence, only differences in δ_{DSS}(dia*) > 0.2 ppm for labile protons of interest (except Tyr58 OH with differences > 0.4 ppm) can be considered significant. Inspection of Table 2 reveals that, upon correction for differences in δ_{dip}, the differences in δ_{DSS}(dia*) between the two complexes for the majority of assigned protons decrease to < 0.2 ppm. Hence, the strength of the majority of H-bonds is conserved during the acid−alkaline transition.

Table 2: Chemical Shift Comparison for Labile Protons in hHO−DMDH−H_2O and hHO−DMDH−OH

	hHO−DMDH−H_2O		hHO−DMDH−OH	
proton	δ_{DSS}(obs)[a]	δ_{DSS}(dia*)[b]	δ_{DSS}(obs)[c]	δ_{DSS}(dia*)[b]
peptide NH				
Tyr58	8.72	8.80	8.94	8.85
Leu93	8.83	8.98	9.03	8.98
Phe95	7.25	7.36	7.40	7.37
Arg85	12.25	12.49	12.83	12.78
Ala110	10.62	10.50	10.48	10.48
Leu164	7.05	7.29	7.25	7.20
Ala165	11.62	11.90	11.78	11.71
Phe166	10.80	11.23	11.23	11.30
Phe167	6.47	7.10	6.97	6.88
side chains				
Tyr58 $O_\eta H$	12.65	13.52	15.50	15.13
Trp96 $N_\varepsilon H$	11.43	11.63	11.49	11.44
Tyr114 $O_\eta H$	11.32	10.72	10.38	10.40
Arg117 $N_\varepsilon H$	9.22	9.11		
Tyr137 $O_\eta H$	10.53	10.66	10.37	10.28
His132 $N_\varepsilon H$	15.04	14.79	14.67	14.75
Tyr182 $O_\eta H$	8.77	8.52	8.50	8.51

[a]Observed chemical shift, in ppm, referenced to DSS via the solvent signal for hHO−DMDH−H_2O in ^1H_2O, 50 mM in phosphate, pH 6.7 at 30 °C. [b]The diamagnetic contribution to the chemical shift that reflects H-bond strength, given by eqs 1 and 3. [c]Observed chemical shift, in ppm, referenced to DSS via the solvent signal for hHO−DMDH−OH in ^1H_2O, 50 mM in carbonate, pH 10.3 at 30 °C.

The distal cavity molecular structure of hHO is strongly conserved upon the loss of substrate (*16*, *23*, *47*, *48*). Important contributions to the structural integrity are sets of H-bonds between two different secondary structural elements (*23*, *48*). Peptide NHs and side chain OHs generally participate in relatively weak H-bonds with $\Delta G \sim 2-7$ kcal/mol (*39*, *40*). Strong H-bonds with $\Delta G \sim 10-25$ kcal/mol, called low-barrier H-bonds (with chemical shifts in the range 17−22 ppm), have been characterized for His ring NHs and side chain OHs that participate in the catalytic mechanism of enzymes (*40*, *41*, *57*). None of the peptide NHs or side chain OHs in hHO complexes (or other HO complexes) belong to this latter class and are considered "weak" H-bonds. However, many residues in hHO exhibit a low-field bias relative to the same functional groups in the overwhelming majority of other proteins (BioMagResBank[2]), indicating that hHO contains several H-bonds that are stronger than the usual "weak" H-bonds. Prominent among these stronger than usual "weak" H-bonds are the Tyr58 OH and Arg136 $N_\varepsilon H$ donors to the carboxylate of Asp140 (Figure 2), the Arg85 and Lys86 peptide NHs and Tyr137 OH donors to the carboxylate of Glu62, the Ala165 and Phe166 peptide NH donors to the carboxylate of Glu92, the His132 and Arg117 $N_\varepsilon H$s donors to the carboxylate of Glu202, and the Ala110 peptide NH and Tyr114 OH donors to the side chain carbonyl of Asn 210.

The deprotonation of the axial water molecule results in the largest changes in the H-bond network for the residue most directly linked to the ligated water molecule. Thus, the Tyr58 OH exhibits δ_{DSS}(dia*) = 12.2 ppm for the aquo complex, whose low-field bias indicates (*40*, *41*, *57*) it is the strongest Tyr H-bond in hHO. Upon deprotonating the ligated water molecule, the Tyr58 δ_{DSS}(dia*) moves further to low field by 1.7 ppm, indicating a

further strengthening of the H-bond. Thus the effect of ligand deprotonation is strongly experienced even for a residue as far as 11 Å from the iron. Unfortunately, it has not been possible to detect the Arg136 $N_\varepsilon H$ signal in the aquo complex (the other donor to Asp140). During the acid−alkaline transition, the H-bond strengths for Ala165 and Phe166 NHs are conserved, the H-bond strengths of Arg85 NH and Tyr137 OH change by ~0.3 ppm in opposite directions, the Lys86 H-bond is conserved, the Tyr114 OH H-bond is slightly weaker, and the Ala110 H-bond strength is conserved. The larger effect on the Arg85/Tyr137 than Ala165/166 H-bond donors upon deprotonation of the water molecule is readily rationalized by the relative proximity of these H-bonds to the strongly altered Tyr58 OH H-bond. Thus, the Tyr137 ring makes strong contacts to both Arg85 and Tyr58. The changes induced in the Arg85/Lys86/Tyr137 H-bonds to Glu62, however, involve a redistribution of the H-bond strength between the residues, not a change in the net H-bond strength. The Lys117 and His132 $N_\varepsilon H$ bonds to Glu202 are relatively distant from the active site and are hence conserved in the acid−alkaline transition.

The effects of ligated water deprotonation on the H-bonding network in HOs have been previously reported (*26*, *27*) only for *Nm*HO. This HO exhibits little sequence homology (*4*) to hHO in the H-bonding network, particularly with respect to the contacts to the conserved, nonligated water molecules in the distal pocket. There are two distal H-bond donors to watered molecules in *Nm*HO (*18*): one (His53 $N_\varepsilon H$) exhibits only ~0.2 ppm change in δ_{DSS}(dia*) and the other (Gln49 $N_\varepsilon H$) exhibits only ~0.5 ppm change in δ_{DSS}(dia*) upon deprotonating the ligated water (*27*). It is thus clear that the distal H-bond network is much more strongly coupled to the axial ligand in hHO than *Nm*HO.

A much more relevant comparison of water deprotonation in hHO would be with *Cd*HO (*19*), whose distal H-bonding network (*24*), as well as the aromatic cluster, is highly homologous to hHO, with Tyr53, Arg132, Gly135, and Asp136 replacing Tyr58, Arg136, Gly139, and Asp140 in hHO (Figure 2). While the assignments necessary to quantitate the magnetic axes and anisotropies for the *Cd*HO complexes are not yet available, a simple pH titration shows that the Tyr53 OH chemical shift changes by a much smaller magnitude (< 0.5 ppm) upon deprotonation of the water molecule[3] than presently observed in the hHO (2.85 ppm) complex. The resonance assignment and magnetic anisotropy/magnetic axes determinations for the respective *Cd*HO complexes will allow a comparison with hHO both in the strength of the Tyr OH → Asp CO_2^- and ligated water molecule → water molecule #1 (Figure 2) H-bonding strength; such a study is in progress.

Implications for the HO Mechanism. Figure 2 depicts the active site structure of hHO−PH−H_2O (*16*), which is very similar to that of the hHO−PH−NO structure in the retention of two ordered water molecules labeled #1 and #2. It is reasonable to assume that the same ordered water molecules are retained in the dioxygen complex, but it is not clear whether ordered water molecule #1 would be retained in the Fe^{3+}−OOH intermediate. The Tyr58 OH chemical shift, and hence its H-bond strength, is strongly modulated by the nature of the axial ligand. Tyr58 is not critical to the HO reaction, (*22*) inasmuch as the Tyr58 → Phe hHO mutant yields biliverdin and does not lead to detectable formation (*22*) of the inactive oxo−ferryl derivative (*7*). However, the rate of biliverdin formation is retarded by a factor of ~2 by this mutation (*22*). The critical role of the Asp140 → Ala mutation that leads (*28*, *29*) to the inactive ferryl group via heterolytic O−O bond cleavage has been attributed to the Asp140 carboxylate serving as a H-bond acceptor to water molecule #1, which, in turn, is then, at best, a weak H-bond donor to the Fe^{3+}−OOH unit. Weak versus strong H-bond donation to the hydroperoxy unit is expected to differentiate between homolytic and heterolytic O−O bond cleavage, respectively. The loss of the Tyr58 OH H-bond would make the Asp140 carboxylate an even stronger H-bond acceptor to ordered water molecule #1 in the mutant. This, in turn, would make ordered water molecule #1 a poorer H-bond donor to the exogenous ligand and hence further favor homolytic over heterolytic bond cleavage, which is consistent with retention of activity in D140A-hHO. At this time, the effect of abolishing the second H-bond to the Asp140 carboxylate (Arg136 $N_\varepsilon H$) is unknown.

It is noted that the only interaction of the Asp140 carboxylate with the active site in mammalian HOs (*16*, *17*) is as a H-bond acceptor for the Tyr58 $O_\eta H$, Arg136 $N_\varepsilon H$, and ordered water molecule #1 (see Figure 2). The retardation of the rate of biliverdin formation upon loss of the Tyr58 $O_\eta H$ H-bond (*22*) argues for this H-bond (and that of Tyr136 $N_\varepsilon H$) having a key role in maintaining the rigid Asp140 carboxylate orientation that optimizes the H-bond with ordered molecule #1, that, in turn, optimizes its H-bond donation to the exogenous ligand.

It is also possible that the Tyr58 OH H-bond is important in steps past the initial stereoselective formation of *meso*-hydroxyheme (Figure 1), such as modulating the proportion of the keto resonance form of *meso*-hydroxyheme that places the radical on the porphyrin ring where it will react with dioxygen, facilitating CO excision (*58*). It would be necessary to compare the rate of formation of each of the three intermediates in Figure 1 for both WT and D140A-hHO to shed additional light on the functional significance of the Tyr58 OH H-bond strength.

[3]Z. Du, M. Ikeda-Saito, and G. N. La Mar, unpublished observations.

ACKNOWLEDGMENT

We thank Dr. Yiming Li for providing the initial 2D NMR spectra for this study.

SUPPORTING INFORMATION AVAILABLE

Seven figures (low-field ^1H NMR spectra, aromatic, aliphatic TOCSY and interaliphatic NOESY for hHO−DMDH−H_2O, and aromatic TOCSY, aromatic NOESY spectra, and magnetic axes for hHO−DMDH−OH) and one table of chemical shifts. This material is available free of charge via the Internet at http://pubs.acs.org.

REFERENCES

1. Tenhunen, R., Marver, H. S., and Schmid, R. (1969) Microsomal heme oxygenase. Characterization of the enzyme. *J. Biol. Chem. 244*, 6388–6394.
2. Ortiz de Montellano, P. R., and Auclair, K. (2003) Heme Oxygenase Structure and Mechanism, in The Porphryin Handbook (Kadish, K. M., Smith, K. M., and Guilard, R., Eds.) pp 175−202, Elsevier Science, San Diego, CA.
3. Wilks, A. (2002) Heme oxygenase: Evolution, structure, and mechanism. *Antioxid. Redox Signaling 4*, 603–614.
4. Frankenberg-Dinkel, N. (2004) Bacterial heme oxygenases. *Antoxid. Redox Signaling 6*, 825–834.
5. Rivera, M., and Zeng, Y. (2005) Heme oxygenase, steering dioxygen activation toward heme hydroxylation. *J. Inorg. Biochem. 99*, 337–354.
6. Unno, M., Matsui, T., and Ikeda-Saito, M. (2007) Structure and catalytic mechanism of heme oxygenase. *Nat. Prod. Rep. 24*, 553–570.

7. Wilks, A., and Ortiz de Montellano, P. R. (1993) Rat liver heme oxygenase—High level expression of a truncated soluble form and nature of the meso-hydroxylating species. *J. Biol. Chem. 268*, 22357–22362.
8. Stocker, R., Yamamoto, Y., McDonagh, A. F., Glazer, A. N., and Ames, B. N. (1987) Biliruben is an antioxidant of possible physiological importance. *Science 235*, 1043–1046.
9. Uzel, C., and Conrad, M. E. (1998) Absorption of heme iron. *Semin. Hematol. 35*, 27–34.
10. Baranano, D. E., and Snyder, S. H. (2001) Neural roles for heme oxygenase: Contrasts to nitric oxide synthase. *Proc. Natl. Acad. Sci. U.S.A. 98*, 10996–11002.
11. Beale, S. I. (1994) Biosynthesis of open-chain tetrapyrroles in plants, algae, and cyanobacteria. *Ciba Found. Symp. 180*, 156–168.
12. Davydov, R. M., Yoshida, T., Ikeda-Saito, M., and Hoffman, B. M. (1999) Hydroperoxy-heme oxygenase generated by cryoreduction catalyzes the formation of α-*meso*-hydroxyheme as detected by EPR and ENDOR. *J. Am. Chem. Soc. 121*, 10656–10657.
13. Kumar, D., de Visser, S. P., and Shaik, S. (2005) Theory favors a stepwise mechanism of porphyrin degradation by a ferric hydroperoxide model of the active species of heme oxygenase. *J. Am. Chem. Soc. 127*, 8204–8213.
14. Wojciechowski, G., and Ortiz de Montellano, P. R. (2007) Radical energies and the regiochemistry of addition to heme groups. Methylperoxy and nitrite radical additions to the heme of horseradish peroxidase. *J. Am. Chem. Soc. 129*, 1663–1672.
15. Chen, H., Moreau, Y., Derat, E., and Shaik, s. (2008) Quantum mechanical/molecular mechanical study of mechanisms of heme degradation by the enzyme heme oxygenase: The strategic function of the water cluster. *J. Am. Chem. Soc. 130*, 1953–1965.
16. Lad, L., Wang, J., Li, H., Friedman, J., Bhaskar, B., Ortiz de Montellano, P. R., and Poulos, T. L. (2003) Crystal structures of the ferric, ferrous and ferrous-NO forms of the Asp140Ala mutant of human heme oxygenase-1: Catalytic implications. *J. Mol. Biol. 330*, 527–538.
17. Sugishima, M., Sakamoto, H., Noguchi, M., and Fukuyama, K. (2003) Crystal structures of CO-, CN-, and NO-bound forms of rat heme oxygenase-1 (HO-1) in complex with heme: Structural implications for discrimination between CO and O_2 in HO-1. *Biochemistry 42*, 9898–9905.
18. Friedman, J. M., Lad, L., Deshmukh, R., Li, H. Y., Wilks, A., and Poulos, T. L. (2003) Crystal structures of the NO- and CO-bound heme oxygenase from *Neisseriae meningitidis*—Implications for O_2 activation. *J. Biol. Chem. 278*, 34654–34659.
19. Hirotsu, S., Chu, G. C., Unno, M., Lee, D.-S., Yoshida, T., Park, S.-Y., Shiro, Y., and Ikeda-Saito, M. (2004) The crystal structures of the ferric and ferrous forms of the heme complex of HmuO, a heme oxygenase of *Corynebacterium diphtheriae*. *J. Biol. Chem. 279*, 11937–11947.
20. Friedman, J., Lad, L., Li, H., Wilks, A., and Poulos, T. L. (2004) Structural basis for novel δ-regioselective heme oxygenation in the opportunistic pathogen *Pseudomonas aeruginosa*. *Biochemistry 43*, 5239–5245.
21. Caignan, G. A., Deshmukh, R., Wilks, A., Zeng, Y., Huang, H.-w., Moenne-Loccoz, P., Bunce, R. A., Eastman, M. A., and Rivera, M. (2002) Oxidation of heme to β- and δ-biliverdin by *Pseudomonas aeruginosa* heme oxygenase as a consequence of an unusual seating of the heme. *J. Am. Chem. Soc. 124*, 14879–14892.
22. Wang, J., Evans, J. P., Ogura, H., La Mar, G. N., and Ortiz de Montellano, P. R. (2006) Alteration of the regiospecificity of human heme oxygenase-1 by unseating of the heme but not disruption of the distal hydrogen bonding network. *Biochemistry 45*, 61–73.
23. Li, Y., Syvitski, R. T., Auclair, K., Wilks, A., Ortiz de Montellano, P. R., and La Mar, G. N. (2002) Solution NMR characterization of an unusual distal H-bond network in the active site of the cyanide-inhibited, human heme oxygenase complex of the symmetric substrate, 2,4-dimethyldeuterohemin. *J. Biol. Chem. 277*, 33018–33031.
24. Li, Y., Syvitski, R. T., Chu, G. C., Ikeda-Saito, M., and La Mar, G. N. (2003) Solution ^{1}H NMR investigation of the active site molecular and electronic structures of the substrate-bound, cyanide-inhibited bacterial heme oxygenase from *C. diphtheriae*. *J. Biol. Chem. 279*, 6651–6663.
25. Liu, Y., Zhang, X., Yoshida, T., and La Mar, G. N. (2004) ^{1}H NMR characterization of the solution active site structure of substrate-bound, cyanide-inhibited heme oxygenase from *Neisseria meningitidis*: Comparison to crystal structures. *Biochemistry 43*, 10112–10126.
26. Liu, Y., Zhang, X., Yoshida, T., and La Mar, G. N. (2005) Solution ^{1}H NMR characterization of the distal H-bond network and the effective axial field in the resting-state, high-spin ferric, substrate-bound complex of heme oxygenase from *N. meningitidis*. *J. Am. Chem. Soc. 127*, 6409–6422.
27. Ma, L.-H., Liu, Y., Zhang, X., Yoshida, T., and La Mar, G. N. (2006) ^{1}H NMR study of the magnetic properties and electronic structure of the hydroxide complex of substrate-bound heme oxygenase from *N. meningitidis*: Influence of the axial water deprotonation on the distal H-bond network. *J. Am. Chem. Soc. 128*, 6657–6668.
28. Koenigs Lightning, L., Huang, H.-W., Moënne-Loccoz, P., Loehr, T. M., Schuller, D. J., Poulos, T. L., and Ortiz de Montellano, P. R. (2001) Disruption of an active site hydrogen bond converts human heme oxygenase-1 into a peroxidase. *J. Biol. Chem. 276*, 10612–10619.
29. Fujii, H., Zhang, X., Tomita, T., Ikeda-Saito, M., and Yoshida, T. (2001) A role for highly conserved carboxylate, aspartate-140, in oxygen activation and heme degradation by heme oxygenase-1. *J. Am. Chem. Soc. 123*, 6475–6484.
30. Matsui, T., Furukawa, M., Unno, M., Tomita, T., and Ikeda-Saito, M. (2005) Roles of distal Asp in heme oxygenase from *Corynebacterium diphtheriae*, HmuO. *J. Biol. Chem. 280*, 2981–2989.
31. Ma, L.-H., Liu, Y., Zhang, X., Yoshida, T., Langry, K. C., Smith, K. M., and La Mar, G. N. (2006) Modulation of the axial water hydrogen-bonding properties by chemical modification of the substrate in resting state, substrate-bound heme oxygenase from *Neisseria meningitidis*: Coupling to the distal H-bond network via ordered water molecules. *J. Am. Chem. Soc. 128*, 6391–6399.
32. Bertini, I., and Luchinat, C. (1996) NMR of paramagnetic substances. *Coord. Chem. Rev. 150*, 1–296.
33. La Mar, G. N., Satterlee, J. D., and de Ropp, J. S. (2000) NMR of Hemoproteins, in The Porphyrins Handbook (Kadish, K. M., Smith, K. M., and Guilard, R., Eds.) pp 185−298, Academic Press, San Diego.
34. Kao, Y.-H., and Lecomte, J. T. J. (1993) Determination of the zero-field splitting constant for proton NMR chemical shift analysis in metaquomyoglobin. The dipolar shift as a structural probe. *J. Am. Chem. Soc. 115*, 9754–9762.
35. Déméné, H., Tsan, P., Gans, P., and Marion, D. (2000) NMR determination of the magnetic susceptibility anisotropy of cytochrome c' of *Rhodobacter capsulatus* by $^1J_{HN}$ dipolar coupling constants measurement: Characterization of its monomeric state in solution. *J. Phys. Chem. B 104*, 2559–2569.
36. Asokan, A., de Ropp, J. S., Newmyer, S. L., and Ortiz de Montellano, P. R. (2001) Solution ^{1}H NMR of the molecular and electronic structure of the heme cavity and substrate binding pocket of high-spin ferric horseradish peroxidase: Effect of His42Ala mutation. *J. Am. Chem. Soc. 123*, 4243–4254.
37. Walker, F. A. (2000) Proton NMR and EPR Spectroscopy of Paramagnetic Metalloporphyrin, in The Porphyrin Handbook (Kadish, K. M., Smith, K. M., and Guilard, R., Eds.) pp 1−183, Academic Press, Boston.
38. Caignan, G. A., Deshmukh, R., Zeng, Y., Wilks, A., Bunce, R. A., and Rivera, M. (2003) The hydroxide complex of *Pseudomonas aeruginosa* heme oxygenase as a model of the low-spin iron(III) hydroperoxide intermediate in heme catabolism: ^{13}C NMR spectroscopic studies suggest the active participation of the heme in macrocycle hydroxylation. *J. Am. Chem. Soc. 125*, 11842–11852.
39. Jeffrey, G. A. (1997) An Introduction to Hydrogen Bonding , Oxford University Press, New York.
40. Harris, T. K., and Mildvan, A. S. (1999) High-precision measurement of hydrogen bond lengths in proteins by nuclear magnetic resonance methods. *Proteins: Struct., Funct., Genet. 35*, 275–282.
41. Mildvan, A. S., Harris, T. K., and Abeygunawardana, C. (1999) Nuclear magnetic resonance methods for the detection and study of low-barrier hydrogen bonds on enzymes. *Methods Enzymol. 308*, 219–245.
42. Zhu, W., Li, Y., Wang, J., Ortiz de Montellano, P. R., and La Mar, G. N. (2006) Solution NMR study of environmental effects on substrate seating in human heme oxygenase: Influence of polypeptide truncation, substrate modification and axial ligand. *J. Inorg. Biochem. 100*, 97–107.
43. Smith, K. M., and Kehres, L. A. (1983) Syntheses of methyl devinylporphyrins related to protoporphyrin-IX. Initial studies on the mechanism of the copper(II) catalyzed cyclizations of 1′,8′-dimethyl-a,c-biladienes. *J. Chem. Soc., Perkins Trans. 1*, 2329–2335.
44. Jeener, J., Meier, B. H., Bachmann, P., and Ernst, R. R. (1979) Investigation of exchange processes by two dimensional NMR spectroscopy. *J. Chem. Phys. 71*, 4546–4553.
45. Griesinger, C., Otting, G., Wüthrich, K., and Ernst, R. R. (1988) Clean TOCSY for ^{1}H spin system identification in macromolecules. *J. Am. Chem. Soc. 110*, 7870–7872.
46. Williams, G., Clayden, N. J., Moore, G. R., and Williams, R. J. P. (1985) Comparison of the solution and crystal structures of mitochondrial cytochrome *c*. Analysis of paramagnetic shifts in the nuclear magnetic resonance spectrum of ferricytochrome *c*. *J. Mol. Biol. 183*, 447–460.

47. Lad, L., Schuller, D. J., Shimizu, H., Friedman, J., Li, H., Ortiz de Montellano, P. R., and Poulos, T. L. (2003) Comparison of the heme-free and -bound crystal structures of human heme oxygenase-1. *J. Biol. Chem. 278*, 7834–7843.
48. Li, Y., Syvitski, R. T., Auclair, K., Ortiz de Montellano, P. R., and La Mar, G. N. (2003) ^{1}H NMR investigation of the solution structure of substrate-free human heme oxygenase: Comparison to the cyanide-inhibited, substrate-bound complex. *J. Biol. Chem. 279*, 10195–10205.
49. Cross, K. J., and Wright, P. E. (1985) Calibration of ring-current models for the heme ring. *J. Magn. Reson. 64*, 220–231.
50. Sandström, J. (1982) Dynamic NMR Spectroscopy , Academic Press, New York.
51. Wüthrich, K. (1986) NMR of Proteins and Nucleic Acids , Wiley & Sons, New York.
52. Neal, S., Nip, A. M., Zhang, H., and Wishart, D. S. (2003) Rapid and accurate calculation of protein ^{1}H, ^{13}C and ^{15}N chemical shifts. *J. Biomol. NMR 26*, 215–240.
53. Sun, J., Wilks, A., Ortiz de Montellano, P. R., and Loehr, T. M. (1993) Resonance Raman and EPR spectroscopic studies on heme heme oxygenase complexes. *Biochemistry 32*, 14151–14157.
54. Brunori, M., Amiconi, G., Antonini, E., Wyman, J., Zito, R., and Rossi-Fanolli, A. (1968) The transition between "acid" and "alkaline" ferric heme proteins. *Biochim. Biophys. Acta 154*, 315–322.
55. Shokhireva, T. K., Shokhirev, N. V., and Walker, F. A. (2003) Assignment of heme resonances and determination of the electronic structures of high- and low-spin nitrophorin 2 by ^{1}H and ^{13}C NMR spectroscopy: An explanation of the order of heme methyl resonances in high-spin feriheme proteins. *Biochemistry 42*, 679–693.
56. Brackett, G. C., Richards, D. L., and Caughey, W. S. (1971) Far-infrared magnetic resonance in Fe(III) and Mn(III) porphyrins, myoglobin, hemoglobin, ferrichrome A, and Fe(III) dithiocarbamates. *J. Chem. Phys. 54*, 4383–4401.
57. McDermott, A., and Ridenour, C. F. (1996) Proton chemical shift measurements in biological solids, in Encyclopedia of NMR, pp 3820−3825, Wiley, Sussex.
58. Liu, Y., Moënne-Loccoz, P., Loehr, T. M., and Ortiz de Montellano, P. R. (1997) Heme oxygenase-1, intermediates in verdoheme formation and the requirement for reduction equivalents. *J. Biol. Chem. 272*, 6909–6917.